Interfacial protein-protein associations

*Blake B. Langdon, Mark Kastantin, Robert Walder, Daniel K. Schwartz**

Department of Chemical and Biological Engineering

University of Colorado Boulder, Boulder, CO 80309

*To whom correspondence should be addressed: daniel.schwartz@colorado.edu

Supporting Information

1. Concentration-dependence of cluster formation provides insight into surface homogeneity

Mapping using accumulated probe trajectories (MAPT), a super-resolution technique developed in our lab, was used to visualize the spatial distribution of adsorbed molecules and associations at the interface.[1] In MAPT different dynamic properties of molecular trajectories (e.g. surface residence time, adsorption, desorption, or association) are grouped using their interfacial positions into two-dimensional bins. The average or cumulative dynamic properties of all trajectory steps within a two-dimensional bin are then calculated. Finally, the accumulated observations for each bin are used to create a 'map' of the surface based on the chosen dynamic property. In these experiments, one movie of 1000 images was acquired over 200 s for each surface site, resulting in 1,000-20,000 accumulated molecular trajectories to construct each MAPT image. Figure S1a-c shows sample MAPT images of BSA_A-BSA_D associations (red pixels) and unassociated BSA_D (gray pixels) for different [BSA_A] solution concentrations. By quantifying the size of each distinct protein association area (i.e. contiguous red pixels where associations occurred, ignoring unassociated proteins), a frequency distribution of apparent protein cluster sizes was constructed for 12 MAPT images at each concentration in Figure S1d.

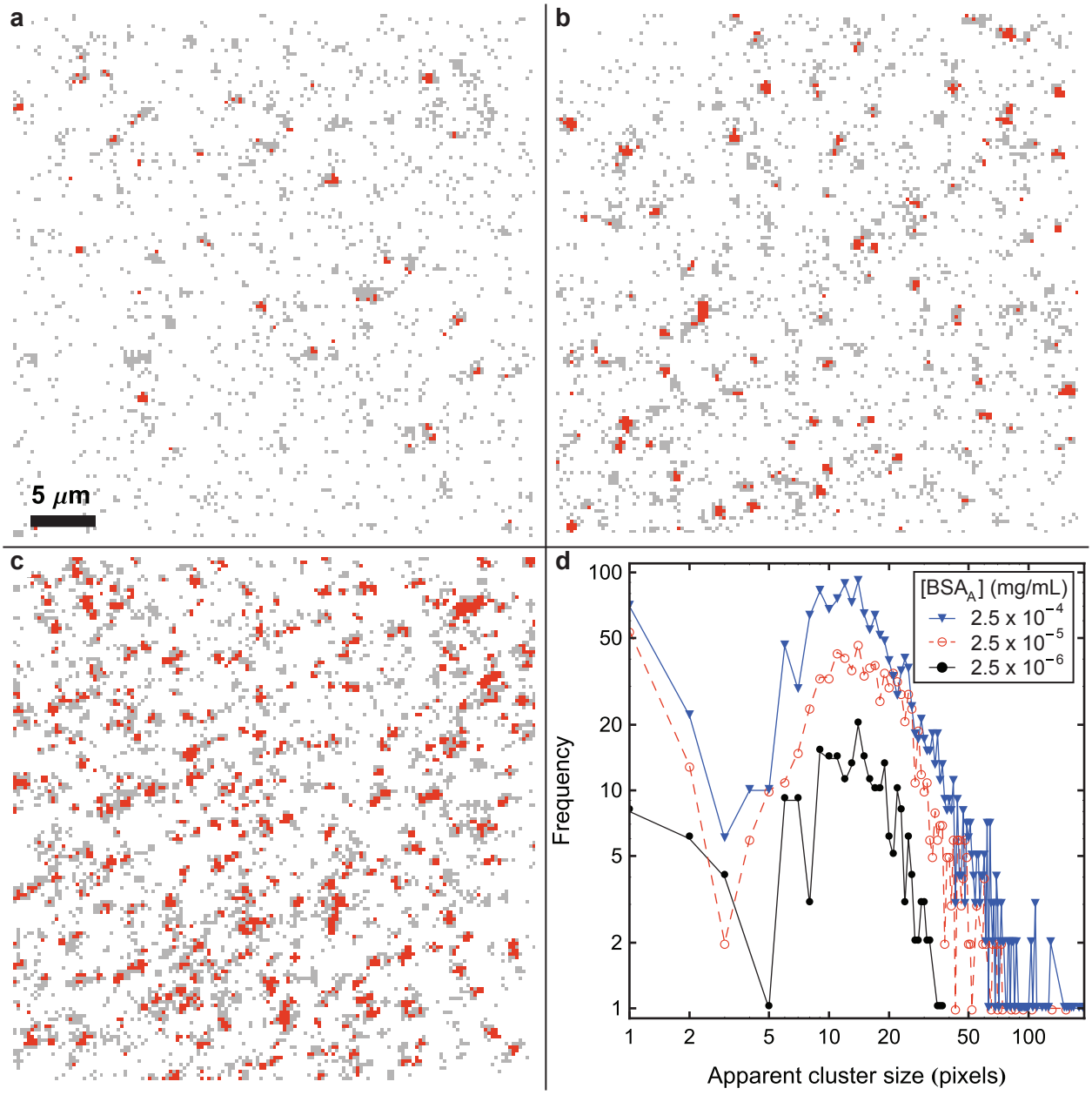

Figure S1. Mapping using accumulated probe trajectories (MAPT) images of BSA_A-BSA_D contacts (red pixels) and unassociated BSA_D (gray pixels) for BSA_A concentrations of (a) $2.5x10^{-4}$ mg/ml, (b) $2.5x10^{-5}$ mg/ml, and (c) $2.5x10^{-6}$ mg/ml. Each pixel in the MAPT images represents one pixel on the EMCCD camera and corresponds to a square area with sides of 227 nm in real space. Each MAPT image represents trajectories collected over a period of 200 s with 0.2 s time resolution. (d) Frequency distribution of apparent cluster sizes is shown for different BSA_A concentrations. Cluster size was quantified in 12 MAPT images, like those shown in (a-c), for each concentration.

Two important conclusions about surface heterogeneity can be drawn from Figure S1. First, while molecules explored some larger contiguous areas, molecules also explored many smaller disconnected areas in Figures S1a-c. If PEG self-assembled monolayer formation were incomplete and contained 'defect sites' of bare fused silica, we would expect proteins to reside preferentially on these 'defect sites' due to favorable interactions with bare fused silica. However, molecules appeared to explore the surface indiscriminately under all conditions. Second, Figure S1d shows that as $[BSA_A]$ increased, the frequency of observing a given apparent cluster size increased and larger apparent cluster sizes were increasingly observed. This indicates that increased $[BSA_A]$ resulted in the formation of clusters at more locations around the surface. In contrast, if aggregation occurred preferentially at special 'defect sites' the frequency of apparent cluster sizes, or number of cluster locations, would be directly related to the surface density of defects, a value that is expected to be independent of $[BSA_A]$. Instead, apparent cluster frequency was concentration-dependent, indicating that the BSA association and dissociation behavior described here was representative of protein behavior on a PEG monolayer and not dominated by defect sites.

2. Observation bias in identifying partial-RET associations

In order to identify objects in each image, a disk matrix image convolution algorithm was performed followed by image thresholding in each channel.[2] Thresholds were selected conservatively such that only diffraction-limited spots above noise were identified as objects. Consequently, objects undergoing partial-RET with similar (and relatively low) F_A and F_D, resulting in average relative distances of ~1, were less likely to be identified in either channel. We hypothesized that the two peaks present in the d_{app} distribution resulted from the identification bias against these objects. In order to test this hypothesis we decreased the identification threshold (by the same fraction in both channels). A larger fraction of neglected objects were identified near d_{app}~1, confirming that the two peaks present in the d_{app} probability distribution were accentuated by the omission of objects with equally low F_A and F_D. While lower thresholds provided better sensitivity to the population at d_{app}~1, they also increased contributions to the data from noise that was anomalously treated as a fluorescent protein; therefore, the lower threshold was not used for results presented elsewhere in this work. Finally, it is important to note that this analysis does not rule out the possibility of multiple RET states in the partial-RET population. However, due to the random labeling scheme used in this work, we could not connect different partial-RET states to different types of BSA-BSA interactions and consequently chose to bin them into a single partial-RET category.

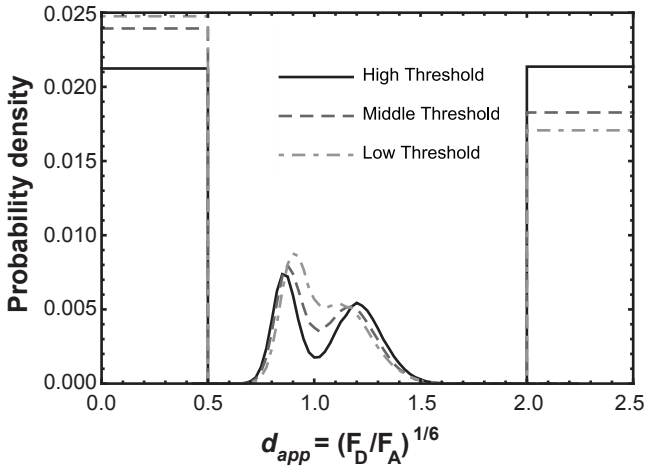

Figure S2. Probability distribution of apparent relative distance, d_{app}, for BSA on PEG at [BSA_A] = $2.5x10^{-4}$ mg/ml. A step function was used to describe the extreme d_{app}-values of the distribution where F_D or F_A was not significantly greater than 0 and d_{app}-value could not be accurately calculated. The object identification threshold for each channel was decreased by 85% (middle) and 66% (low) from the threshold used to identify objects for these experiments (high).

3. Donor fluorophore photobleaching

When using fluorescent labels, photobleaching on time scales relevant to dynamic observations can lead to erroneous interpretations. For example, photobleaching of donor fluorophores attached to a BSA_D molecule would be treated as a desorption event when in fact the molecule may remain at the interface. Similarly, for associating BSA_D-BSA_A molecules the deactivation of donor fluorophores would be treated as both an apparent desorption event and an apparent dissociation event. Ultimately photobleaching has the potential to shorten the surface residence times and contact times measured in these experiments. Fluorophore photobleaching would only significantly affect our results if it occurred on a time scale comparable to or shorter than the physical time scales being measured. In order to assess the effect of photobleaching, the first-order time constant for donor fluorophore photobleaching was quantified by measuring the apparent surface residence time distribution of BSA_D molecules that were covalently attached to the surface. The apparent desorption of immobilized proteins results solely from donor photobleaching.

Fused silica wafers were cleaned by piranha exposure, drying, and UV-ozone treatment as described in materials and methods. A monolayer of 3-glycidoxypropyltrimethoxysilane (GPTMS) was then deposited on cleaned fused silica wafers by vapor deposition using a solution of toluene (85%), GPTMS (10%), and *n*-butylamine (5%) for 24 h at room temperature. BSA_D molecules were immobilized on the GPTMS monolayer through the reaction of the epoxide ring of GPTMS with primary amines on lysine residues, as described previously.[5] The GPTMS monolayer was exposed to a solution of BSA_D ($[BSA_D]=10^{-7}$ mg/mL) at pH 9.0 with 150mM sodium chloride. After 20 h, any unreacted BSA_D molecules were removed with a series of vigorous solvent rinses including deionized water, toluene, isopropanol, and acetone. Finally, wafers were exposed to a deionized water bath at 50ºC.

The apparent surface residence times were then measured using SM-TIRFM tracking for the immobilized BSA_D molecules under the same buffer solution, laser power, and filter conditions used elsewhere in the work. Several time-lapse series of images, taken at 1 s intervals, were acquired while the laser remained on continuously. After image processing and object identification and tracking, the apparent surface residence times for all immobile molecules were used to create an apparent residence time cumulative distribution (Figure S3). This distribution exhibited a mono-exponential decay with a characteristic photobleaching time constant of 57 ± 2 s. The measured photobleaching time constant was at least an order of magnitude longer than the mean characteristic surface residences time for associating molecules (1.11 ± 0.04 s for $[BSA_A] = 2.5x10^{-5}$ mg/ml) and two orders of magnitude longer than the mean characteristic contact time (0.25 ± 0.03 s for $[BSA_A] = 2.5x10^{-4}$ mg/ml), indicating that photobleaching had a negligible effect on the results presented in this work.

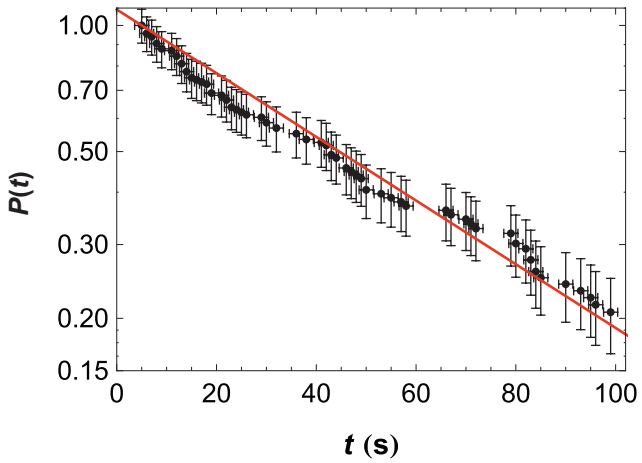

Figure S3. Apparent cumulative surface residence time distribution of immobilized BSA_D when illuminated by 532nm. Molecules were covalently attached to the surface such that apparent desorption was the result of photobleaching.

4. Interfacial diffusion promotes cluster formation

Single-molecule tracking enables the measurement of molecular diffusion by tracking a molecule's movement from frame-to-frame. By default, interfacial diffusion is expected to follow two-dimensional Gaussian random-walk statistics. As with previous studies of protein interfacial diffusion, an object may diffuse via multiple diffusion modes – each characterized by a diffusion coefficient, D_j – during its time on the surface.[2,6,7] The cumulative squared-displacement distribution can be modeled simply by the sum of the cumulative distributions for each mode weighted by the fraction of observed steps, f_j, corresponding to that mode:

$$C(R^2, \Delta t) = \sum_j f_j e^{-R^2/4D_j\Delta t}$$

where R^2 is the squared-displacement for the time interval Δt. The average diffusion coefficient, $\overline{D}$, can then be calculated as the fraction-weighted average of each mode:

$$\overline{D} = \sum_j f_j D_j$$

Figure S4a shows a cumulative squared-displacement distribution of all steps observed for all trajectories. On this log-linear graph, a single diffusive mode would appear linear. Instead several modes

were present with 48 ± 2% of steps coming from a diffusive mode characterized by a diffusion coefficient of 0.0151 ± 0.0004 $\mu m^2/s$. This diffusion coefficient essentially represents the apparent movement of immobile objects due to imperfect spatial localization.[8] Two mobile diffusive modes were also observed, with 46 ± 2% and 6.8 ± 0.2% of steps belonging to modes characterized by diffusion coefficients of 0.047 ± 0.001 $\mu m^2/s$ and 0.243 ± 0.004 $\mu m^2/s$, respectively (Table S1). On average BSA_D molecules exhibited a diffusion coefficient of 0.045 ± 0.001 $\mu m^2/s$, indicating significant interfacial mobility. We estimated that a single BSA_D molecule collides with BSA_A molecules at a frequency of ~1 s^{-1} for a surface coverage of 25 BSA_A molecules per μm^2 at a $[BSA_A] = 2.5x10^{-4}$ mg/ml.

Another way to understand a molecule's interfacial mobility is to consider the total Euclidean distance between a molecule's initial adsorption position to its final desorption position. As shown in Figure S4b, many molecules move significantly from their initial adsorption position; e.g. ~10% of molecules moved more than 1 μm, which is more than 100 molecular lengths of BSA.

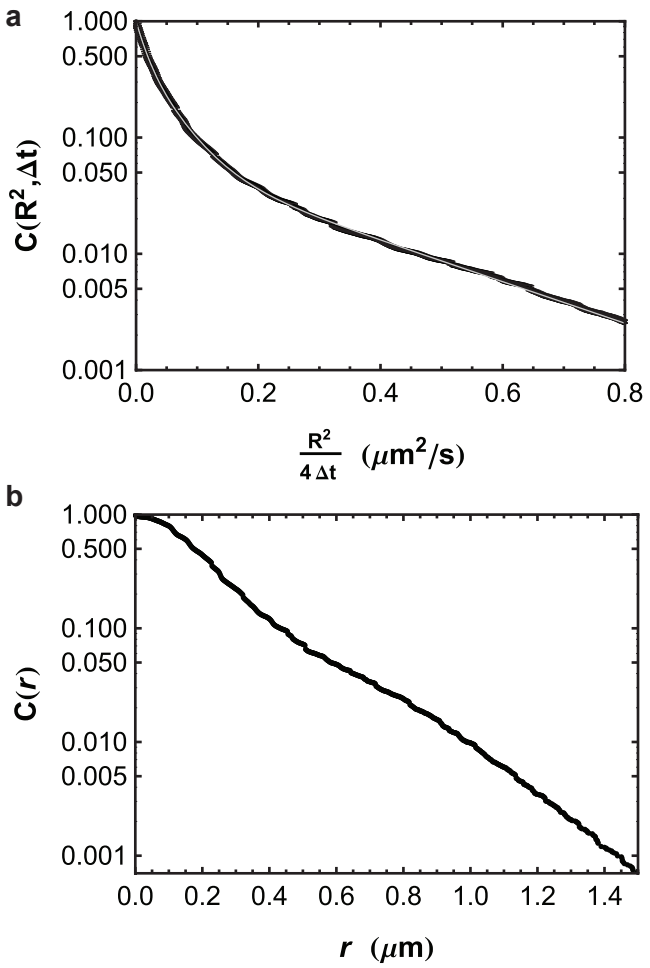

Figure S4. (a) Cumulative squared-displacement distribution of all trajectory steps at $[BSA_A]$ = $2.5x10^{-5}$ mg/ml with multimodal diffusion. The mode fractions and diffusion coefficients corresponding to the fit shown in gray are presented in Table S1. (b) Cumulative distribution of surface displacements over the course of each trajectory's surface residence time (i.e. the Euclidean distance between adsorption and desorption positions) at $[BSA_A]$ = $2.5x10^{-5}$ mg/ml.

Table S1. Diffusion mode fractions and diffusion coefficients for $[BSA_A]$ = $2.5x10^{-5}$ mg/ml shown in Figure S4a.

mode	f_j	D_j (μm^2/s)
1	0.48(2)	0.0151(4)
2	0.46(2)	0.047(1)
3	0.068(2)	0.243(4)

References

(1) Walder, R.; Nelson, N.; Schwartz, D. K. *Nat. Commun.* **2011**, *2*.

(2) Walder, R.; Schwartz, D. K. *Langmuir* **2010**, *26*, 13364–13367.

(3) Berney, C.; Danuser, G. *Biophys. J.* **2003**, *84*, 3992–4010.

(4) Lakowicz, J. R. In *Principles of Fluorescence Spectroscopy*; Lakowicz, J. R., Ed.; Springer New York, 2006; pp. 443–475.

(5) McLoughlin, S. Y.; Kastantin, M.; Schwartz, D. K.; Kaar, J. L. *Proc. Natl. Acad. Sci.* **In Press**. DOI: 10.1073/pnas.1311761110

(6) Kastantin, M.; Langdon, B. B.; Chang, E. L.; Schwartz, D. K. *J. Am. Chem. Soc.* **2011**, *133*, 4975–4983.

(7) Langdon, B. B.; Kastantin, M.; Schwartz, D. K. *Biophys. J.* **2012**, *102*, 2625–2633.

(8) Kastantin, M.; Schwartz, D. K. *Microsc. Microanal.* **2012**, *18*, 793–7.